



# Hyperdiffusion of dust particles in a turbulent tokamak plasma

F. Nespoli, I. Kaganovich, A. Autricque, P. Tamain, Y. Marandet

## ► To cite this version:

F. Nespoli, I. Kaganovich, A. Autricque, P. Tamain, Y. Marandet. Hyperdiffusion of dust particles in a turbulent tokamak plasma. *Physics of Plasmas*, 2021, 28 (7), pp.073704. 10.1063/5.0051332 . hal-03663972

HAL Id: hal-03663972

<https://amu.hal.science/hal-03663972>

Submitted on 10 May 2022

**HAL** is a multi-disciplinary open access archive for the deposit and dissemination of scientific research documents, whether they are published or not. The documents may come from teaching and research institutions in France or abroad, or from public or private research centers.

L'archive ouverte pluridisciplinaire **HAL**, est destinée au dépôt et à la diffusion de documents scientifiques de niveau recherche, publiés ou non, émanant des établissements d'enseignement et de recherche français ou étrangers, des laboratoires publics ou privés.

# Hyperdiffusion of dust particles in a turbulent tokamak plasma

F. Nespoli<sup>1</sup>, I.D. Kaganovich<sup>1</sup>, A. Autricque<sup>2</sup>, Y. Marandet<sup>3</sup>, P. Tamain<sup>2</sup>,

<sup>1</sup> Princeton Plasma Physics Laboratory, 100 Stellarator Road, Princeton, NJ 08540, United States of America

<sup>2</sup>IRFM, CEA Cadarache, F-13108 St. Paul-lez-Durance, France

<sup>3</sup>Aix Marseille Univ, CNRS, PIIM UMR 7345, Marseille, France

Email: [fnespoli@pppl.gov](mailto:fnespoli@pppl.gov)

## Abstract

The effect of plasma turbulence on the trajectories of dust particles is investigated for the first time. The dynamics of dust particles is computed using the ad-hoc developed Dust Injection Simulator code, using a 3D turbulent plasma background computed with the TOKAM3X code. As a result, the evolution of the particle trajectories is governed by the ion drag force, and the shape of the trajectory is set by the Stokes number  $St \propto a_d/n_0$ , with  $a_d$  the dust radius and  $n_0$  the density at the separatrix. The plasma turbulence is observed to scatter the dust particles, exhibiting a hyperdiffusive regime in all cases. The amplitude of the turbulent spread of the trajectories  $\Delta r^2$  is shown to depend on the ratio  $Ku/St$ , with  $Ku \propto u_{rms}$  the Kubo number and  $u_{rms}$  the fluctuation level of the plasma flow. These results are compared with a simple analytical model, predicting  $\Delta r^2 \propto (Ku/St)^2 t^3$ , or  $\Delta r^2 \propto (u_{rms} n_0/a_d)^2 t^3$ . As the dust is heated by the plasma fluxes, thermionic emission sets the dust charge, originally negative, to slightly positive values. This results in a substantial reduction of the ion drag force through the suppression of its Coulomb scattering component. The dust grain inertia is then no longer negligible, and drives the transition from a hyperdiffusive regime towards a ballistic one.

---

## 1 Introduction

Sub-millimeter dust particles are ubiquitous in magnetic confinement fusion experiments, being generated by the interaction of the plasma with the solid surfaces, due to erosion or melting of the latter, from constant material migration and re-deposition [1] or transient heat and particle fluxes [2]. Dust can penetrate in the confined plasma seriously polluting it, eventually resulting in a radiative collapse (stellarators) or even disruption (tokamaks), posing a hazard to the safe operation of the device. Dust particles can also be a source of tritium retention for a fusion reactor, and its in vessel inventory must be limited for the nuclear safety of the facility. Recently, impurity injection in the form of sub-millimeter powder grains has also been used for wall conditioning and plasma control purposes in both tokamaks [3, 4, 5] and stellarators [6, 7]. Furthermore, the injection of (sub)millimeter-sized fragments of material with the Shattered Pellet Injection is proposed as a disruption mitigation mechanisms for ITER [8].

Modeling the dynamics of dust particles in a fusion plasma is therefore crucial for both the safe operation of a fusion reactor and for the interpretation of experiments employing powder grains. Great efforts have been undertaken in this direction in the recent past, and several codes computing the evolution of dust three-dimensional (3D) trajectories have been developed, such as DUSTT [9, 10], DUSTRACK [11, 12], MIGRAINe [13, 14], DTOKS [15], and DUMBO [16, 17]. This problem includes both plasma and material physics, and is highly non-linear. So far, all existing investigations of dust dynamics employed time-independent background plasma profiles computed from transport codes, in 2D for axisymmetric devices and in 3D for stellarators [18]. The effects of plasma turbulence on dust dynamics are therefore usually neglected, or at best modeled with random

scattering, set by an arbitrary parameter [9]. Fusion plasmas though can be strongly turbulent, especially in the plasma edge and scrape-off layer (SOL), where dust particles can survive due to lower heat fluxes from the plasma.

In this work, we investigate for the first time the effects of plasma turbulence on dust dynamics. We employ a dust tracking algorithm developed ad hoc on the base of the existing numerical models, using a self-consistent 3D turbulent plasma background computed using the plasma fluid turbulence code TOKAM3X [19]. The numerical model used in the investigation is described in section 2, and more in detail in the appendix. An example of dust trajectory in the turbulent plasma is detailed in section 3, where in particular we show how thermionic emission can set the dust charge to values close to zero, resulting in a substantial reduction of the ion drag force, and a transition towards inertia-dominated trajectories. The effects of turbulence on dust dynamics are estimated from the scattering of trajectories in section 4, showing how dust particles hyperdiffuse in the turbulent plasma, until the dust grain inertia becomes important, eventually transitioning towards a ballistic regime. In section 5, we show how the turbulent scattering depends mainly on two adimensional numbers, the Kubo and the Stokes number. In section 6 we compare our results with a simple model. Finally, summarize the results and we discuss the implications for plasma fusion experiments and their modeling.

## 2 Numerical model

Starting from existing dust trajectories computing codes, we developed a dedicated algorithm to assess the effect of turbulence on dust dynamics, the Dust Injection Simulator (DIS). In particular, following Refs. [9, 11], DIS solves for four equations: i) Newton's motion equation in 3D

$$m_d \frac{d\mathbf{v}}{dt} = \mathbf{R}_f \quad (1)$$

with  $m_d$  the mass of the dust grain and  $\mathbf{R}_f$  the sum of the forces acting on it ii) current balance (dust charge)

$$I_{tot}(\chi, T_d) = 0 \quad (2)$$

with  $I_{tot}$  the total current flowing to the dust grain,  $\chi = -e\Phi_d/T_e$  the normalized dust electric potential and  $T_d$  the dust surface temperature iii) dust temperature evolution

$$m_d c_p \frac{dT_d}{dt} = W_{tot} \quad (3)$$

with  $W_{tot}$  the total heat flux and  $c_p$  the thermal capacity iv) dust grain mass evolution

$$\frac{dm_d}{dt} = m_I \Gamma_{tot} \quad (4)$$

with  $\Gamma_{tot}$  the net particle flux to/from the dust, and  $m_I$  the mass of the atoms composing the dust particle. Indeed, while for a sub-millimeter dust grain the charging time is typically negligible with respect to the time resolution used in dust tracking simulations, the thermal equilibration time is not [9] and  $T_d$  can not be simply inferred from heat flux balance. When a dust material which can exhibit a liquid phase is considered, an additional equation is solved instead of Eq. (3) under the condition  $T_d = T_m$ , with  $T_m$  the melting temperature, to determine the melted fraction  $f_m$ :

$$m_d h_m \frac{df_m}{dt} = W_{tot} \quad (5)$$

where  $h_m$  is specific heat of fusion. In the simulations exposed in this paper though, we consider the dust grains to be composed of carbon (C). This assumption, relevant for most existing magnetic fusion experiments, also allows us to make some simplifying assumptions, such as neglecting dust melting and ferromagnetic forces, that have to be considered for metallic dust. The main force acting on the dust grains, i.e. the ion drag force  $\mathbf{F}_d$ , and the ion and electron fluxes from the plasma and the associated heat fluxes, used for determining the dust charge state and temperature respectively, are derived in the framework of orbital motion limited (OML) theory [20]. A necessary assumption of the OML theory is that the dust grain is spherical. For this reason, we neglect effects such as the rocket force [21], arising in case of asymmetrical evaporation of the heated dust, and which can be of the same order of magnitude as  $\mathbf{F}_d$ , since it requires asymmetrical dust shapes or somehow uneven heating of the dust.

In the following we briefly discuss the various terms considered in Eqs.(1-4), namely the forces, currents, particles and heat fluxes on the dust grain. The expressions for these quantities, taken mainly from Refs. [9, 10, 17] are then detailed in the appendix. In Eq. (1), we consider the following forces acting on the dust:

$$\mathbf{R}_f = \mathbf{F}_d + \mathbf{F}_{d,n} + \mathbf{F}_E + \mathbf{F}_g + \mathbf{F}_c \quad (6)$$

The main force is the ion drag force  $\mathbf{F}_d = \sum_z \mathbf{F}_{d,z}$  given by the sum of the drag forces for each different ion species  $z$ . Each of these components can be written as

$$\mathbf{F}_{d,z} = m_{i,z} n_{i,z} \pi a_d^2 v_{T,i,z} \zeta \left( \frac{u_z - v}{v_{T,i,z}}, Z\chi \right) (\mathbf{u}_z - \mathbf{v}) \quad (7)$$

with  $\mathbf{u}_z$  the background ion flow velocity,  $n_{i,z}$ ,  $v_{T,i,z}$  and  $m_{i,z}$  the ion density, thermal velocity and mass respectively for the ion species  $z$  with charge  $Z$ , and  $a_d$  is the dust grain radius. The complex function  $\zeta \left( \frac{u_z - v}{v_{T,i,z}}, Z\chi \right) \sim 5$ , derived in the framework of the OML theory and detailed in the appendix, is the sum of two contributions, due to the collection of plasma ions and to their Coulomb scattering with the charged dust grain respectively,  $\zeta = \zeta_{coll} + \zeta_{sc}$ . The scattering part usually dominates, and strongly depends on the dust electric potential as  $\zeta_{sc} \propto (Z\chi)^2$ . The drag force from neutrals  $\mathbf{F}_{d,n}$  has a similar expression, but can typically be neglected with respect to  $\mathbf{F}_d$ , since the net neutral flow is, in most situations, negligible with respect to the plasma flow  $u_n \ll u$  and the neutral density is small compared to the plasma density  $n_n/n_e \ll 1$ , except in cases such as a detached divertor or in presence of neutral beam injection heating the plasma.  $\mathbf{F}_E = q_d \mathbf{E}$  is the electric force on the dust grain with charge  $eq_d/a_d = \chi T_e$ ,  $\mathbf{F}_g = m_d g$  is gravity, and  $\mathbf{F}_c = m_d (-v_\phi^2/R, 0, v_R v_\phi/R)$  is the centrifugal (apparent) force, arising in our cylindrical frame of reference  $(R, Z, \phi)$ . We are now interested just in the first passing of the dust grains into the plasma, therefore we also neglect dust collisions and reflections on the wall.

The electric charge of the dust is determined by Eq. (2), which reads

$$I_i + I_e + I_{th} + I_{SEE} = 0. \quad (8)$$

Here,  $I_i = \sum_z I_{i,z}$  and  $I_e$  are the ion and electron currents, respectively. We consider thermionic electron emission from the heated dust  $I_{th}$  and secondary electron emission  $I_{SEE}$  as charging mechanisms. Thermionic and secondary electron emission are important since, depending on the dust and plasma temperature, can change the sign of the dust charge. Though, we neglect here secondary effects such as electron back scattering [14] and recombination of magnetized re-emitted electrons [22]. We also neglect electron currents due to photo emission, which can be important in other contexts such as astrophysical dusty plasmas, but is typically orders of magnitude smaller than  $I_e$  in tokamak environment [10], except in the case where the dust grain dwells in a region of the vacuum vessel

that is not directly in contact with the plasma.

The evolution of dust temperature  $T_d$  is determined in Eq. (3) by the total heat flux  $W_{tot}$ , which reads

$$W_{tot} = W_i + W_e + W_p - W_{ev} - W_{bb} - W_{th} - W_{SEE} \quad (9)$$

The heat fluxes associated with the kinetic energy of impinging ion and electron fluxes, heating the dust grain, are respectively  $W_i$  and  $W_e$ .  $W_p = I_i E_p$  accounts for the neutralization of ions on the dust surface, with  $E_p = 13.6$  eV for hydrogen. The heat fluxes associated with the loss of electrons through thermionic emission  $W_{th}$ , and secondary electron emission  $W_{SEE}$ , contribute to cooling the dust grain, together with the radiative cooling  $W_{bb}$ . The heat flux  $W_{ev}$ , associated with the evaporation particle flux  $\Gamma_{ev}$  from the heated dust surface, also reduces the surface temperature.

Finally, the evaporation flux is the only term we consider in Eq. (4),

$$\Gamma_{tot} = -\Gamma_{ev} \quad (10)$$

since all other impurity fluxes (sputtering, re-deposition) are typically orders of magnitude smaller than the evaporation flux (sublimation in the case of graphite dust).

The equations solved by DIS are expressed in dimensionless units to conform to the plasma background. In particular, distances are in units of the ion sound speed Larmor radius  $\rho_s$  and time is in units of  $\omega_c^{-1}$ , being  $\omega_c$  the electron cyclotron frequency, and the mass dust is normalized to its value at  $t = 0$ .

We remark that drag forces resulting from impurity ions can be comparable to the drag force given by the main plasma ion, being  $F_{d,z} \propto n_{i,z} \sqrt{m_{i,z}} Z^2$ , since the function  $\zeta$  in Eq. (7) varies with the ion charge  $Z$  approximately as  $\zeta(Z\chi) \propto Z^2$ . Nevertheless, in the simulations exposed in this paper we will consider only the main plasma ions, assumed to be deuterium, with no impurities. Similarly, charging currents from impurities are also neglected. This choice is driven, apart from the attempt of excluding unnecessary complexities from this first investigation, by the fact that our turbulent background plasma does not include a description of impurities or neutrals. For the same reason, the drag force from neutrals is here also set to zero.

Indeed, the turbulent plasma background is computed using the TOKAM3X code [19]. TOKAM3X is a fluid turbulence, flux-driven code, based on drift-reduced Braginskii equations for the plasma edge and SOL. The code solves the continuity equation, the parallel momentum balance equation, the electron parallel motion in the form of a generalized Ohms law and the charge conservation equation ( $\nabla \cdot j = 0$ ), and energy balance equations for electrons and ions separately [23]. The time-averaged profiles and their fluctuations are determined self-consistently by turbulence as the system is driven by incoming particle and energy fluxes. The  $\mathbf{E} \times \mathbf{B}$  velocity is included in the evaluation of the plasma flow used in the computing the dust dynamics. TOKAM3X can model realistic magnetic geometries, including X-points. Nevertheless, for the investigation exposed in this paper, we decided to avoid unnecessary complexities and employed the easiest (yet realistic) plasma geometry: a circular cross section plasma, limited at the HFS midplane. The size of the simulation is comparable to a medium size tokamak being  $a/\rho_s = 325$  with  $a$  the minor radius. The simulation domain covers half of the torus with the resolution of  $64 \times 512 \times 64$  points in the  $r, \theta, \phi$  directions. The simulation results are normalized in terms of a typical density and temperature  $n_0$  and  $T_0$ , representative of the values of  $n$  and  $T_e$  at the LCFS. While  $n_0$  enters DIS proportionally through all terms related to plasma fluxes,  $T_0$  also sets the physical size of the system through  $\rho_s$  (together with the magnetic field on axis  $B_0$ ). Furthermore, the plasma temperature influences material properties (directly and indirectly through the dust temperature  $T_d$ ) such as SEE, thermionic emission, sublimation flow, radiation cooling. In our investigation we set therefore the values  $n_0 = 0.5 \cdot 10^{19} m^{-3}$ ,  $T_0 = 40$  eV,  $B_0 = 1$  T. This choice of  $T_0$  and  $B_0$  set the Larmor

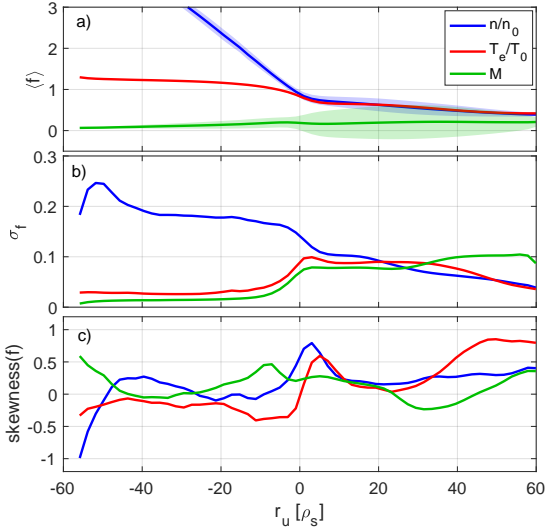


Figure 1: Radial profiles of a) average plasma density (blue), electron temperature (red) and parallel Mach number (green), b) fluctuation level and c) skewness for the same quantities. The shaded area shows the variation in the poloidal plane.

radius and cyclotron frequency to  $\rho_s = 0.91$  mm and  $\omega_c = 6.8 \cdot 10^7$  s $^{-1}$ . In the following, time will be expressed in units of  $\omega_c^{-1}$ , the conversion to second being  $10^5 \omega_c^{-1} = 1.5$  ms. The value of  $n_0$ , not affecting the spatial and temporal scales of the simulation, will be used to re-scale the simulations results to investigate different Stoke numbers, as it will be detailed in section 5.

As it will be verified a posteriori, dust particles have trajectories lasting around 20 ms. To contain computational costs, the typical turbulence simulations only extend a few milliseconds. To cover arbitrary long dust trajectories, we cycle over the TOKAM3X simulation results in time, under the assumption that, at steady state, the turbulent fluctuations are quasi-periodic. The time window  $[t_i, t_f]$  to be repeated has been chosen as a trade off between minimizing the overall differences in between the simulation fields at  $t = t_i$  and  $t = t_f$ , while maximizing the extent of the usable simulation  $t_f - t_i$ . This resulted in  $t_f - t_i \sim 1.6$  ms. This procedure altered the turbulence auto-correlation time  $\tau_c$ , computed as the volume average over the SOL of auto-correlation time of the plasma parallel flow  $\Gamma_i = n u_i$  individually computed for each grid cell, by only 0.12%. Indeed, as verified a posteriori, the variations of the plasma quantities introduced by this procedure are not distinguishable from the ones experienced by dust particle during its trajectory, which are given by turbulence itself (see inlet of Fig. 3, where we plot the plasma quantities probed by a dust grain during its trajectory over a time interval  $\Delta t > 3(t_f - t_i)$ ).

In Fig. 1a we show the radial profiles of average plasma quantities  $\langle f \rangle$ , where  $f = n/n_0$ ,  $T_e/T_0$ ,  $M$  in blue, red, green respectively, brackets denote average over poloidal and toroidal direction and time. Here,  $M = u_i/c_s$  is the Mach number, with  $u_i$  the velocity of the plasma ions and  $c_s$  the ion sound speed. The shaded area shows the variation of these quantities in the poloidal direction. The upstream radial coordinate  $r_u$  is 0 at the LCFS. The profiles of the fluctuations  $\sigma_f$  (absolute value) of the same quantities are shown in Fig. 1b. For all shown quantities, the relative fluctuation level is  $\sigma_f/\langle f \rangle \sim 0.15$  in the SOL, except for  $M$  which assumes values close to 0, in which case the relative fluctuation level is not a meaningful measurement. The skewness of these quantities in shown in Fig. 1c exhibits positive values outside the LCFS, which, together with a positive value of excess kurtosis (not shown here), indicates the presence of intermittent turbulent transport. A

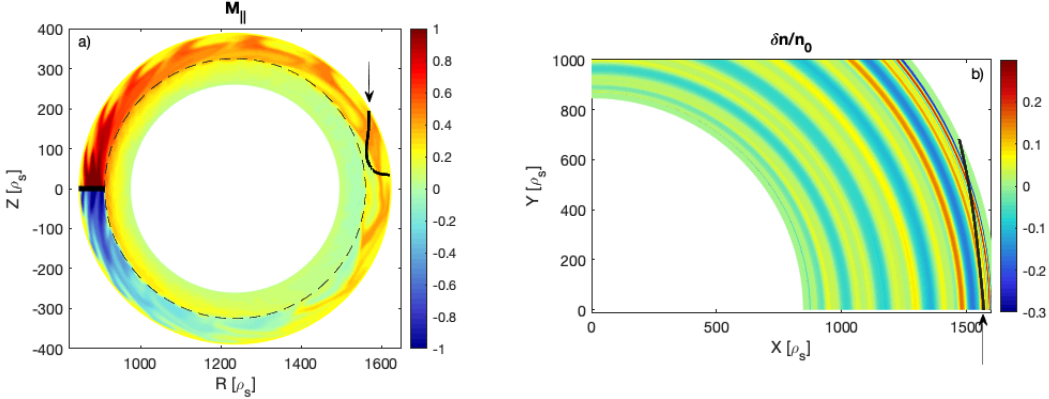


Figure 2: Poloidal (a) and top (b) projection of an example dust trajectory (black line), together with a snapshot of the the parallel mach number  $M_{||}$  (a) and density fluctuation  $\delta n/n_0$  (b) resulting from TOKAM3X simulations. The injection point is indicated by black arrows. The LCFS is shown with a black dashed line. The limiter is shown with a thick black line.

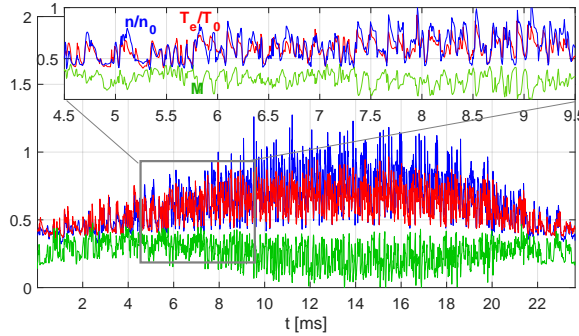


Figure 3: Time traces of plasma density (blue), electron temperature (red) and toroidal Mach number (green) experienced by the dust grain in the trajectory shown in Fig. 2, with a zoom on part of the trajectory.

more detailed analysis of the statistical properties of turbulence for similar TOKAM3X simulations can be found in Ref. [24].

### 3 Example of dust grain trajectory

Different types of trajectory are possible depending on the initial conditions. In this study, we avoid this additional degree of freedom by fixing the initial condition: the dust grain is injected into the plasma from the external radial boundary of the simulation at the poloidal position  $\theta = 30^\circ$ . The dust grain has an initial velocity directed downwards,  $\mathbf{v}_0 = v_0 \mathbf{e}_z$ , with  $v_0 = -10$  m/s. This scenario mimics impurity powder injection experiments [3, 4, 5, 6]. The chosen poloidal position maximizes the dwelling of the dust grains into the plasma, while ensuring that the trajectory is contained in the SOL and does not cross the LCFS, where the turbulence characteristics are qualitatively different from the SOL. Indeed, the turbulence fluctuation level and its skewness are usually measured in the experiments to be reduced inside the LCFS with respect to the SOL [25], as it can also be seen in our simulations Fig. 1b-c. As an example, a trajectory for the case  $a_d = 5\mu\text{m}$  is shown in Fig. 2. Black lines in subplots a and b show, respectively, the projections of the trajectory onto the

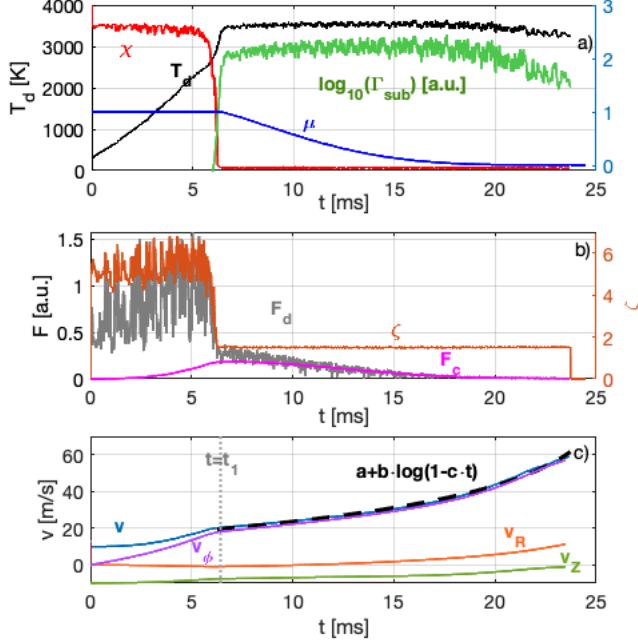


Figure 4: Time traces relative to the trajectory in Fig. 2. a) Dust temperature  $T_d$  (black, left axis), normalized electric potential  $\chi$  (red, right axis) and mass  $\mu$  (blue, right axis), and sublimation flux  $\Gamma_{\text{sub}}$  (green). b) Ion drag force  $F_d$  (grey), apparent centrifugal force  $F_c$  (magenta), and the function  $\zeta$  (orange, right axis). c) Total dust velocity  $v$  (blue) and its  $R, Z, \phi$  components, fit with Eq. (12) (black,dashed).

poloidal plane ( $R, Z$ ) and on the ( $X, Y$ ) plane (top view), together with a snapshot of the parallel Mach number  $M_{\parallel}$  (a) and of the density fluctuation on a flux surface (b). The variation of the plasma parameters experienced by the dust grain during its trajectory is shown in Fig. 3. Here the rapid variation of the quantities due to plasma turbulence is visible, and is better resolved in the zoomed part plotted in the inlet.

The time traces of the trajectory in Fig. 2 are plotted in Fig. 4. Initially, the particle is dropped from the top of the plasma and falls vertically through the SOL. The dust grain is negatively charged ( $\chi \sim 2.5$ ), (Fig. 4a, red). The main force here is the ion drag force  $F_d$  (Fig. 4b, grey), fluctuating because of turbulence, which is directed along the field lines, i.e. predominantly in the toroidal direction. The dust grain is then accelerated in the toroidal direction, and its velocity (Fig. 4c, blue) increases mainly through its toroidal component  $v_{\phi}$  (violet), and so does the apparent centrifugal force  $F_c$  (Fig. 4b, magenta) due to the dust grain inertia. As the dust grain enters the SOL and probes a denser and hotter plasma, its temperature  $T_d$  (Fig. 4a, black) increases. When the dust grain reaches sufficiently high temperatures ( $t > t_1 \sim 6.45$  ms), the thermionic emission becomes important, setting the dust electric potential to negligible values  $\chi \lesssim 0$ . This in turns reduces the ion drag force  $F_d$  by a factor of five, through the function  $\zeta(\frac{u-v}{v_{T,i}}, \chi)$ . We remind that

$\zeta$  is the sum of a collection and scattering contributions,  $\zeta = \zeta_{\text{coll}} + \zeta_{\text{sc}}$ , with the scattering part  $\zeta_{\text{sc}} \propto \chi^2$  usually dominating. The suppression of dust charge down to  $\chi \sim 0$  driven by thermionic emission results therefore in the almost complete suppression of the scattering contribution to the drag force, leaving only the contribution due to collection. This results in a five-fold reduction of  $\zeta$  and  $F_d$ , which eventually becomes comparable to or even smaller than the centrifugal force  $F_c$ . The

motion of the dust grains will be at this stage governed by their inertia, moving almost tangentially to the torus (see Fig. 2b).

When the temperature is high enough for the thermionic emission to dominate the charge balance, the dust grain starts to sublime. The heat flux associated with the growing sublimation flux  $\Gamma_{sub}$  (Fig. 4a, green) sets now the dust temperature to values close to the sublimation point. As a result, the (normalized) dust mass  $\mu$  (Fig. 4a, blue) starts to decrease, eventually resulting in the complete evaporation of the dust grain towards the end of the trajectory. Accordingly, the forces  $F_d$  and  $F_c$  decrease. Though, while  $F_c$  is directly proportional to  $\mu$ ,  $F_d \propto a_d^2 \propto \mu^{2/3}$ . This results in a growing acceleration as the mass decreases  $F_d/\mu \propto \mu^{-1/3}$ . As the dust grain evaporates, the evolution of the mass  $\mu$  is described by Eq. (4), with  $\Gamma_{tot} = \Gamma_{sub} \propto a_d^2 \propto \mu^{2/3}$ . We consider now the second part of the trajectory  $t \geq t_1$  (vertical dotted line in Fig. 4c), where the dust temperature  $T_d$  is kept approximately constant by the evaporation heat flux. The evaporation flux can then be approximated as  $\Gamma_{sub} = C_{sub}\mu^{2/3}$ , with  $C_{sub}$  being a constant (see appendix). The dust dynamics is described here by the equations

$$\frac{d\mu}{dt} = -\mu^{2/3}C_{sub}, \quad \frac{dv}{dt} = \mu^{-1/3}C_d \quad (11)$$

where  $C_d = F_d/\mu^{2/3}$  is the part of the drag force independent of the dust mass (radius). Approximating  $C_d$  to also be constant for simplicity, this results finally in a velocity growing accordingly to

$$v(t) = v_1 - \frac{3C_d}{C_{sub}} \ln \left[ \frac{\mu_1^{1/3} - (C_{sub}/3)(t - t_1)}{\mu_1^{1/3}} \right] \quad (12)$$

with  $v_1 = v(t = t_1)$  and  $\mu_1 = \mu(t = t_1) = 1$ . As it is shown in figure Fig. 4c, the dust grain velocity (blue) is well fitted by Eq. (12) (black dashed line).

## 4 Hyperdiffusion of dust grains in a turbulent plasma

In systems governed by turbulence, or in general by random collision, the spread of test particles evolves as  $\Delta r^2(t) \propto t^\gamma$ . Depending on the value of the exponent  $\gamma$ , different transport regimes are possible: while the case  $\gamma = 1$  corresponds to normal diffusion,  $\gamma < 1$  and  $\gamma > 1$  gives rise to subdiffusion and superdiffusion respectively, the latter approaching the ballistic regime for  $\gamma = 2$ . When the spread of test particles evolves even faster,  $\gamma > 2$ , hyperdiffusion takes place. To investigate the effect of plasma turbulence on dust dynamics we compute the trajectories of a set of dust grains with the same initial conditions (position, velocity), but with a different turbulence phase for the background plasma. The turbulence phase is changed by randomly selecting the initial toroidal position  $\phi_i$ , and the initial time with respect to the turbulent TOKAM3X simulation,  $t_i$ . This choice is motivated by the fact that, in experimental conditions, both variables are unknown when injecting a powder particle into the plasma. For our TOKAM3X simulation, 64 values of  $\phi_i$  are available. To reduce computational costs while maintaining a sufficient time resolution for turbulent fluctuations, the TOKAM3X simulations have been re-sampled by a factor 4, finally leading to 267 possible values for  $t_i$ . We consider therefore an ensemble of 300 particles, differing only by the values of  $\phi_i$ ,  $t_i$ . We characterize then the spread of the position  $\Delta r^2$  as a function of time. Here, we compute  $\Delta r^2$  as the standard deviation of the three-dimensional position  $\mathbf{r}$  of the ensemble of particles.

As a first investigation, we compute a set of trajectories for different dust grain sizes:  $a_d = [0.1, 0.3, 0.75, 1.5, 5, 15, 50] \mu\text{m}$ . The dust trajectories in the turbulent plasma are shown

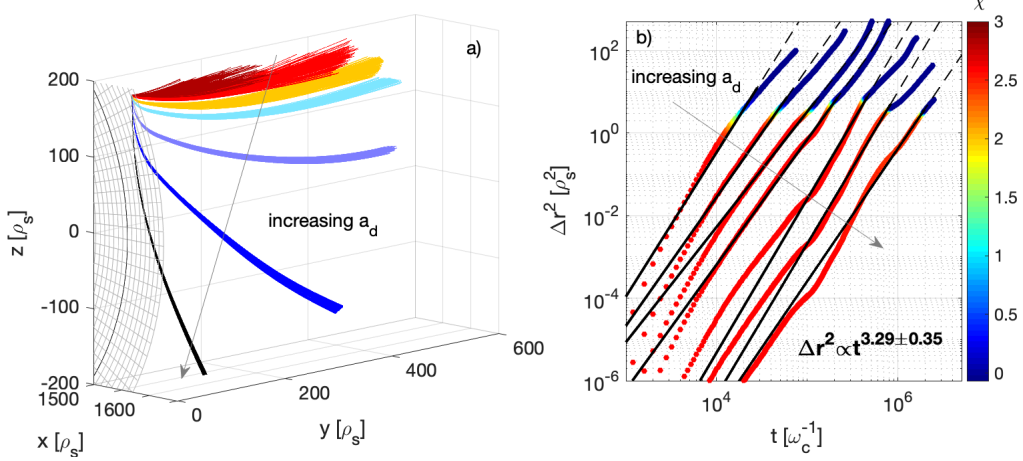


Figure 5: a) Dust trajectories for different values of dust radius  $a_d \in [0.1, 100]\mu\text{m}$ . b) Evolution of the turbulent spread  $\Delta r^2(t)$  for the trajectories in a), color coded with the normalized electric potential  $\chi$ . Fit with  $\Delta r^2(t) = (t/t_0)^\gamma$  is shown with black lines. ( $10^5\omega_c^{-1} = 1.5\text{ ms}$ )

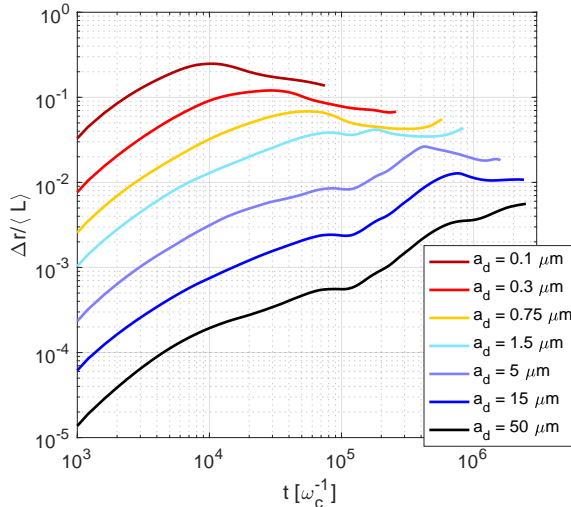


Figure 6: Evolution of the ratio of the mean displacement  $\Delta r$  to the mean trajectory length  $\langle L \rangle$  for the same cases as in Fig. 5.

in Fig. 5a with different colors for different values of  $a_d$ . The corresponding evolution of the turbulent spread  $\Delta r^2(t)$  is shown in Fig. 5b, color coded with the normalized electric potential  $\chi$ . Here, black lines show the fit  $\Delta r^2(t)$  of with

$$\Delta r^2(t) = (t/t_0)^\gamma \quad (13)$$

where  $t_0$  is the time needed for having  $\Delta r = \rho_s$ . As it emerges from the picture, the turbulent spreading is more significant for small dust grains, becoming almost negligible for the highest value of  $a_d$ , where  $\Delta r \geq \rho_s$  only in the end of the trajectory. This is made clearer in Fig. 6, where we plot the ratio of the mean displacement  $\Delta r$  to the mean trajectory length  $\langle L \rangle$  for the same cases as in Fig. 5. The turbulent spread can be as high as 25% of the trajectory length for the smallest dust case  $a_d = 0.1\mu\text{m}$ , while it remains always  $< 1\%$  for the biggest dust considered  $a_d = 50\mu\text{m}$ . In

all cases though, initially the dust particles are in a hyperdiffusive regime, with  $3 \lesssim \gamma \leq 4$ , as it will be detailed later. For most of the trajectories, a sharp change in slope of  $\Delta r^2(t)$  is observed when  $\chi$  is set to values close to zero by thermionic emission, resulting generally speaking in a reduction of  $\gamma$ , being  $2 \leq \gamma \leq 4$ , getting closer to a ballistic regime.

Hyperdiffusion has been observed to emerge in the framework of generalized Langevin equations, especially in the case of a "tilted washboard" potential in Ref. [26, 27]. The tilted washboard potential, where particles are subject to a periodic potential biased by a constant force  $V = -V_0 \cos(2\pi x/x_0) - Fx$ , exhibits a strong similarity with our case, at least qualitatively. Indeed, in the hyperdiffusive phase ( $\chi > 0$ ) the main force acting on the dust particle is the ion drag force, Eq. (7), which locally oscillates in both space and time around a mean value (even though without a well defined frequency/ wave number as in the washboard potential case). When the drag force dominates, our problem is equivalent to a Langevin equation for Brownian motion [28]

$$\dot{\mathbf{r}} = \mathbf{v}, \quad \dot{\mathbf{v}} = \eta_d(\mathbf{u} - \mathbf{v}) \quad (14)$$

with  $\eta_d$  the Stokes dumping rate and  $\mathbf{u}$  the background flow. This equation is used to describe the dynamics of turbulent aerosols, such as water droplets in clouds or dust in interstellar gas [29]. This problem can be parameterized with two adimensional numbers: the Stokes and Kubo number. They quantify, respectively, the importance of the particle inertia with respect to the background flow, and the level of turbulence of such flow:

$$St = 1/(\eta_d \tau_c), \quad Ku = u_{rms} \tau_c / \lambda \quad (15)$$

where  $\tau_c$  is the correlation time of the turbulent flow,  $u_{rms}$  is the rms amplitude of the turbulent flow fluctuations and  $\lambda$  is their typical size. In our case, we consider  $\tau_c = 1343\omega_c^{-1}$  the auto-correlation time of the plasma flow fluctuations as defined previously in sec. 2, and  $\lambda = \sqrt{A_b/\pi} = 18.8\rho_s$ , where  $A_b$  is the average blob poloidal area, computed using the blob recognition and tracking algorithm detailed in Ref. [30]. This results in  $Ku = 5.48$  for our turbulent simulation. Conversely, the dumping rate is

$$\eta_d = 3m_i n_0 v_{T_i} \zeta / (4a_d \rho_d) \quad (16)$$

so that  $St \propto a_d/n_0$ .

The velocity of the dust particles  $v$ , typically  $< 10^2$  m/s, is negligible with respect to the background plasma flow  $u$ , of the order of  $10^4$  m/s. We separate the plasma drag  $\eta_d \mathbf{u}$  into a background, average component plus the turbulent fluctuations. As shown in Fig. 2b, typically the relative variations of the plasma density  $n$  (and therefore of  $\eta_d$ ) are smaller than the ones of the parallel flow  $M_{||}$ . We can then, in first approximation, assume constant  $\eta_d$ . We can rewrite Eq. (14) as

$$\dot{\mathbf{r}} = \mathbf{v}, \quad \dot{\mathbf{v}} = \langle \eta_d \mathbf{u} \rangle + \delta(\eta_d \mathbf{u}) \quad (17)$$

where brackets denote ensemble averaging, and  $\delta$  refers to the variation with respect to the ensemble-average value. The turbulent spreading of the bunch of particles can then be computed in the framework of a statistical solution of the Langevin Equation, as explained in detail in Ref. [31, 32]. If we assume that the diffusive process takes place, instead of the real space, in the velocity space, with the velocity of the single particles receiving random "kicks"  $\delta a = \delta(\eta_d \mathbf{u})$  due to turbulence. In this case, the spread in the velocity space  $\Delta v^2$  is described by

$$\Delta v^2 = \int_0^t dt' \int_0^t dt'' \langle \delta a(t') \delta a(t'') \rangle \quad (18)$$

First, we consider the stochastic acceleration variations in between different trajectories to be uncorrelated, so that the two point correlation function  $C(t', t'') = \langle \delta a(t') \delta a(t'') \rangle = 2D_v \delta(t' - t'')$ , with  $D_v$  the diffusion coefficient in the velocity space. This results in diffusion of velocities,  $\Delta v^2 = 2D_v t$ , resulting in a spread in real space evolving as  $\Delta r^2 = 8/9 D_v t^3$ .

We remark that, in general, for long time scales compared to the viscous damping in the Langevin equation (which term we have neglected in this case moving from Eq. (14) to Eq. (17) since  $v \ll u$ ), the two point-correlation function  $C(t', t'')$  depends only on the time difference  $\tau = t'' - t'$ . In this case,  $D_v$  is then related exactly to the rms value of the acceleration fluctuations by  $D_v = a_{rms}^2 \tau_{ac}^L$ , with  $\tau_{ac}^L = C(0)^{-1} \int_0^\infty d\tau C(\tau)$  the Lagrangian auto-correlation time [32].

By using the approximations  $a_{rms} = \delta(\eta_d u)_{rms} \sim \eta_d u_{rms}$  and  $\tau_{ac}^L \sim \tau_c$  the auto-correlation time defined previously in sec. 2, and the definition in Eq. (16), the spatial spread can be rewritten as

$$\Delta r^2 = \frac{1}{2} \left( \frac{m_i n_0 v_{Ti} \zeta u_{rms}}{a_d \rho_d} \right)^2 \tau_c t^3 \quad (19)$$

or, alternatively, in terms of Kubo and Stokes number as

$$\Delta r^2 = 2 \left( \frac{2Ku\lambda}{3St} \right)^2 \left( \frac{t}{\tau_c} \right)^3 \quad (20)$$

This equation describes well, in terms of both time evolution and governing parameters, the observed turbulent spreading of the dust particles, as it will be detailed in the following section. Though, as already mentioned, we observe values of  $3 \leq \gamma < 4$ , so a faster spreading than predicted by Eq. (20). This can be understood in the following way: in our investigation, we inject dust particles from the top of the plasma through the scrape-off layer. The dust particles falls through a progressively denser plasma, and experiences an ion drag force  $F_d \propto n$  increasing in time (Fig. 4b). Accordingly, the fluctuations of  $F_d$  increase in time. In this case, the implicit assumption that  $D_v$  is constant in space/time used in the derivation Eq.(20) is no longer true. The temporal dependence of  $\delta(\eta_d u)_{rms}$  is the result of several factors, such as i) the exponential decay of density with distance from the LCFS in the SOL ii) initial dust velocity and direction iii) non trivial spatial distribution of the parallel velocity fluctuation level in the SOL. Then, when computing  $\Delta r^2$  by time integrating  $\Delta v^2$ , the variation in time of  $D_v$  has to be taken into account, resulting in a more accurate (but less general) estimate of  $\Delta r^2$ , than Eqs. (19, 20).

We remark that in our case, the velocity of the dust grain is negligible with respect to the velocity of the structures of the background turbulence. Indeed, the blob structures are typically traveling outwards, self-propelled by internal  $\mathbf{E} \times \mathbf{B}$  drift. In our case, the average blob radial velocity is computed by a tracking algorithm [30] to be  $v_r = 0.022c_s$ . The spatial and temporal variations of the turbulence, as experienced by the dust particle, can then not be disentangled, and therefore the dependency on  $\lambda$  and  $\tau_c$  in Eq. (20). In the following, we will use  $St$  and  $Ku$  as governing parameters, though they have to be intended as a proxy of  $a_d/n_0$  and  $u_{rms}$  respectively. An additional investigation on the eventual dependency on  $\lambda$  and  $\tau_c$  is left for future works.

## 5 Scaling of turbulent spreading

To investigate the dependencies of the dust spreading, and in particular of the parameters  $\gamma$  and  $t_0$  in Eq. (13), on the governing parameters  $St$  and  $Ku$ , we perform a series of dust-tracking simulations where i) we scan  $St$  through the dust radius  $a_d = [0.1, 0.3, 0.75, 1.5, 5, 15, 50] \mu\text{m}$  ii) and through the plasma density  $n_0 = [0.2, 1, 5, 20, 80] \cdot 10^{18} \text{ m}^{-3}$  iii) similarly to what has been done in Ref. [33], we artificially alter  $Ku$  by transforming the turbulent plasma fields  $f$  into

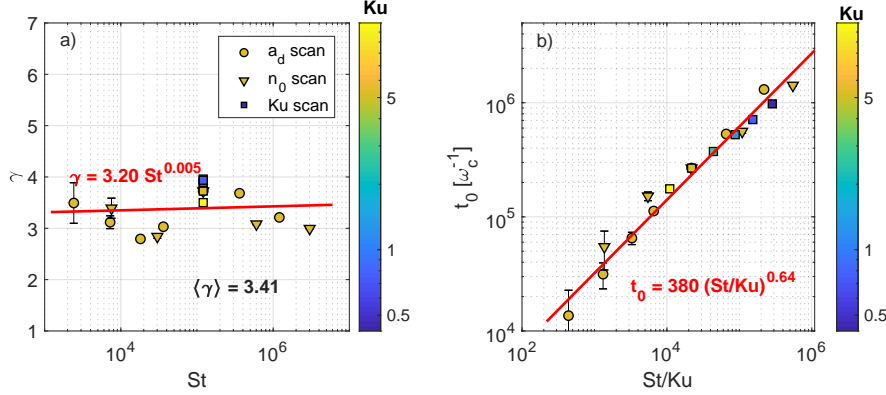


Figure 7: Dependence of a)  $\gamma$  and b)  $t_0$  on  $Ku$  and  $St$ , for the  $a_d$  scan (circles),  $n_0$  scan (triangles), and  $Ku$  scan (squares), color coded with  $Ku$ . Best fit with  $y = ax^b$  are shown with red lines for the part of the trajectory in which  $\chi > 0$ . ( $10^5 \omega_c^{-1} = 1.5$  ms)

$\langle f \rangle + (f - \langle f \rangle)/(N_{Ku} + 1)$ , with  $f = \{n, T_e, T_i, M_{||}, \Phi\}$ , bracket defines average over time and the toroidal direction, and  $N_{Ku} = [-0.5, 0, 1, 3, 6, 12]$ . We remark that changing  $St$  through  $n_0$  is not self-consistent, as in reality changing the value of the density would alter the plasma collisionality, which in turn would change the turbulence properties such as the size of the turbulent structures, as discussed in detail in Ref. [24]. Though, this method allows us to perform a first investigation of the role of  $St$  while containing the computational cost. A more self-consistent study is foreseen for future works.

As a first result, changing  $n_0$  has qualitatively the same effect on trajectories as the one shown in Fig. 5a by changing  $a_d$ , i.e. at fixed  $a_d$ , trajectories in a more tenuous plasma are equivalent to trajectories of bigger dust particles, and trajectories in a denser plasma are equivalent to the ones of smaller dust particles, confirming that  $St \propto a_d/n_0$  is indeed the governing parameter of this problem. We analyze then separately the turbulent spreading for the two different parts of the trajectories, defined by  $\chi > 0$  (dust negatively charged) and  $\chi \leq 0$  (dust positively charged), separately fitting them with Eq. (13) to extract the parameters  $\gamma$  and  $t_0$ . The results of the fit as a function of  $St$  and  $Ku$  are summarized in Figs. 7 and 8 for the  $\chi > 0$  and  $\chi < 0$  parts of the trajectory, respectively.

We discuss first the initial part of the trajectories,  $\chi > 0$  (Fig. 7). Here, hyperdiffusion is observed in all cases, being always  $\gamma \gtrsim 3$ , with average value 3.41. The results obtained by scanning the plasma density  $n_0$  (triangles) and the dust radius  $a_d$  (circles) are qualitatively the same, and  $\gamma$  is observed to have overall no dependence on  $St$ , the results being well fit by  $\gamma \propto St^{0.005}$  (red line in Fig. 7a). Decreasing the Kubo number slightly increases  $\gamma$ , being comprised in between 3.5 and 3.94 for the highest and lower  $Ku$  values in the  $Ku$  scan respectively (squares in Fig 7a). Conversely,  $t_0$  is observed to increase with  $St$  and decrease with  $Ku$ . We remark that, from Eq. (13), at a given time  $t$ ,  $\Delta r^2 \propto t_0^{-\gamma}$ . This result therefore means that the turbulent spreading is decreased for increasing  $St$ , consistently with what shown in Fig 5, where  $St \propto a_d$ , and it is increased with  $Ku$ , that gives a measure of how turbulent the background flow is. The two dependencies can be combined, and  $t_0$  is well described by  $t_0 \propto (St/Ku)^{0.64}$ . These results are consistent with the simple analytical model described in section 4, as it will be detailed later.

We consider now the second part of the trajectory,  $\chi < 0$  (Fig. 8). First, we remark that not all the trajectories exhibit this part: for the highest  $St$  (big particles or low plasma density), the heat flux collected by the dust particle is not enough for the thermionic emission to dominate and

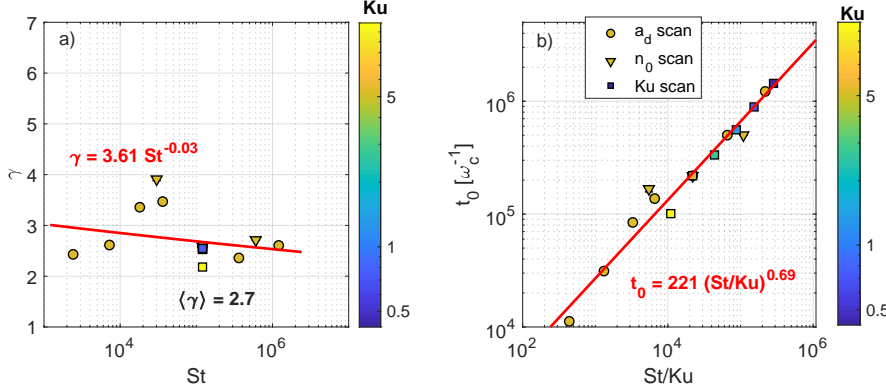


Figure 8: Dependence of a)  $\gamma$  and b)  $t_0$  on  $Ku$  and  $St$ , for the  $a_d$  scan (circles),  $n_0$  scan (triangles), and  $Ku$  scan (squares), color coded with  $Ku$ . Best fit with  $y = ax^b$  are shown with red lines for the part of the trajectory in which  $\chi < 0$ . ( $10^5 \omega_c^{-1} = 1.5$  ms)

reduce the dust charge to values close to zero. At intermediate-high  $St$  values, the second part of the trajectory is dominated by the particle inertia, as explained in section 3. Here,  $\gamma \gtrsim 2$ , getting close to the case of ballistic diffusion. For lower  $St$  numbers, the value of  $\gamma$  is sometimes increased, exhibiting once again an hyperdiffusive behaviour  $3 < \gamma < 4$  even in this phase. As a general trend, the variation of  $\gamma$  with  $St$  is well described by  $\gamma \propto St^{-0.03}$ , and almost no effect on  $\gamma$  is observed by changing  $Ku$ .  $t_0$  shows a similar behaviour as in the hyperdiffusive phase, Depending on both  $St$  and  $Ku$ , and being well described by  $t_0 \propto (St/Ku)^{0.69}$ .

Before analyzing further our results, we discuss here the validity of the OML theory for our parameter spaces. Indeed, the OML theory, which provides the main force and charging mechanism considered in our model, is derived under the assumptions of small grain  $a_d/\lambda_D \ll 1$  with  $\lambda_D$  the Debye length, unmagnetized and collisionless plasma.

- Dust size: for our reference case ( $a_d = 5 \mu\text{m}$ ,  $n_0 = 5 \cdot 10^{18} \text{ m}^{-3}$ ),  $a_d/\lambda_D \sim 1/5$  through all the trajectory. Since  $\lambda_D \sim \sqrt{n_e}$ , for this case and lower  $St$  (smaller grains, higher density) the OML theory is valid. For higher  $St$ , this is not strictly true. Though, following Ref. [9], we included in the computation of the Coulomb logarithm a factor  $\eta_{fit}$ , which is meant to extend the validity of the OML drag force to bigger grains, by fitting the the results from Ref. [34]. Here, PIC simulations of charging/forces on a spherical object are performed in the limit  $a_d > \lambda_D$ . In the same article, the author compares the surface potential given by the PIC simulations with the OML prediction, finding a good agreement in a wide range of  $a_d/\lambda_D$ . We can then consider our approach reasonable for all  $St$  values under this perspective.
- Magnetization: the OML expressions are derived for an unmagnetized plasma. The effect of magnetization has been investigated for example in Ref. [35] and [36]. In Ref. [35], numerical simulations of dust charging in a magnetized plasma are performed. The deviation from the OML charging has been found to be "not significant" for  $a_d/\rho_L < 1$ , with  $\rho_L$  the Larmor radius. In Ref. [36], numerical simulations of ion drag force on a dust grain in magnetized plasma are performed. The authors find that magnetization reduces the drag force, but it remains substantially unvaried for  $a_d/\rho_L < 0.1$ . Both this conditions are satisfied in our case, being  $\rho_s = 0.91 \text{ mm}$  and  $a_d \leq 50 \mu\text{m}$ .
- Collisionality: OML expressions are derived for collisionless plasma. This might not be true

especially in the dense cloud of atoms ablated from the dust [37]. In Ref. [38], the authors compute the maximal dust radius where OML still holds depending on the plasma conditions  $n_e$ ,  $T_e$ . In the case of C grains, and for our reference case, the maximal radius is  $a_{max} \lesssim 10\mu m$ . The condition  $a_d < a_{max}$  is therefore satisfied for the reference case and smaller radii, while it is not for bigger dust grains and for denser plasma, so the simulation results might not be accurate in this situation from a collisionality point of view. Models of dust shielding by the ablated vapor cloud have been developed for the case of high-Z materials such as tungsten (W) [39, 40] and applied to DUSTT simulations of W dust trajectories [41], but are not yet available for lower-Z material such as C, so at present our model is still the best approximation we can have in this scenario.

## 6 Discussion

In this work, we presented an investigation of the effect of plasma turbulence on the dynamics of dust particles in a tokamak environment, using 3D turbulent background plasma provided by the TOKAM3X code. When the ion drag force dominates, all the studied cases exhibit an hyperdiffusive behaviour, where the spatial spread of a bunch of particles evolves in time as  $\Delta r^2 = (t/t_0)^\gamma$ , with  $3 \leq \gamma \leq 4$ , while the dust grain is negatively charged  $\chi > 0$ . When the heat fluxes collected by the dust grain are sufficient, the thermionic emission dominates the charging process setting the dust charge to negligible values  $\chi \lesssim 0$ . In this case, the dynamics of the dust particle is governed by their inertia, and the spreading evolves slower in time,  $2 \leq \gamma \leq 4$ , getting close to a ballistic case for bigger particles, while still exhibiting hyperdiffusion for the smaller grains. The observed hyperdiffusive regimes can be recovered from a statistical solution of Langevin equation, to which our problem can be reduced when the ion drag force dominates, and being parametrized by the adimensional Stokes and Kubo numbers,  $St \propto a_d/n_0$  and  $Ku \propto u_{rms}$ . Assuming the diffusive process occurs in the velocity space, the limit case  $\gamma = 3$  corresponds to velocity diffusion. In this case, a simple model has been derived for the hyperdiffusive spreading Eqs. (19, 20), giving a general prediction  $\Delta r^2 \propto (Ku/St)^2 t^3$ , or  $\Delta r^2 \propto (u_{rms} n_0/a_d)^2 t^3$ . Spreading faster than  $\Delta r^2 \propto t^3$  is due to the details of the investigated case, in particular to the spatial variations of plasma quantities such as density and flow velocity, and of their fluctuations. This model is qualitatively consistent with the results presented in section 5, and in particular with the results shown in Fig. 7. Here, the turbulent spreading was found to be well described by  $\Delta r^2 = (t/t_0)^\gamma$  with  $t_0 \propto (St/Ku)^{0.64}$  and  $\gamma \sim 3.41$ , that would result in  $\Delta r^2 \propto (Ku/St)^{2.18} t^{3.41}$ .

More precisely, the turbulent spreading of dust particles can be described by an empirical scaling law with  $St$  and  $Ku$  derived from our simulations:

$$\begin{aligned}\gamma &= 3.20 St^{0.005}, \quad t_0 \omega_c = 380(St/Ku)^{0.64} \quad (\chi > 0) \\ \gamma &= 3.61 St^{-0.03}, \quad t_0 \omega_c = 221(St/Ku)^{0.69} \quad (\chi \leq 0)\end{aligned}\tag{21}$$

Concluding, we showed how plasma turbulence can scatter dust particles under the action of the ion drag force, resulting in hyperdiffusion of the dust particles. Such effect can be beneficial for powder injection/SPI experiments, as they can help spreading the impurity source on a wider plasma volume. The amplitude of the turbulent scattering can become important for low Stokes numbers (up to 25% of the trajectory length for small particles and/or high density plasma), and might not be negligible even for moderate dust sizes for fusion reactor relevant densities, and should therefore be taken into account. When expensive turbulence simulations are not available, the turbulent scattering provided by a model or empirical scaling similar to the ones exposed in this paper could be included when using a plasma background computed using transport codes. Though, dedicated

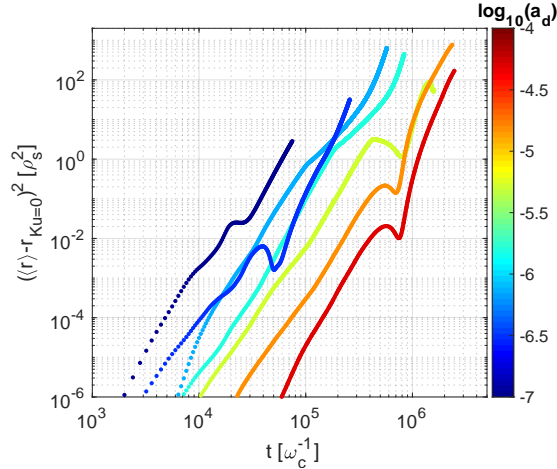


Figure 9: Time traces of deviation of the mean turbulent trajectory with respect to the case computed using a non-turbulent, 2D-and-time-averaged background plasma,  $\langle r \rangle - r_{Ku=0}$ , for the same cases as in Fig. 5, color coded with the dust radius. ( $10^5 \omega_c^{-1} = 1.5 \text{ ms}$ )

simulation of dust trajectories in turbulent plasmas will be needed first, in order to extend our results to plasmas with specific shapes, and for different injection points for the dust particles. Furthermore, the deviation of the mean turbulent trajectory with respect to the case computed using a non-turbulent, 2D-and-time-averaged background plasma,  $\langle r \rangle - r_{Ku=0}$  can be comparable or bigger than the turbulent  $\Delta r$ . The time evolution of  $(\langle r \rangle - r_{Ku=0})^2$  is plotted in Fig. 9 for the  $a_d$  scan, to be compared with  $\Delta r^2$  plotted in Fig. 5 for the same cases. Indeed, due to the non-linearity of the problem, the ensemble-averaged dust trajectories does not coincide with the trajectory computed using the 2D plasma background (averaged over time and toroidal direction), and  $\langle r \rangle - r_{Ku=0}$  can be of the same order of magnitude as  $\Delta r^2$ , while exhibiting a more complex time evolution and dependence on the dust radius. This investigation though is outside the scope of this work, and calls for the use of turbulent plasma background for a more consistent evaluation of the dust trajectories.

## Acknowledgments

The authors would like to thank Prof. John Krommes for fruitful discussion. This work is supported by the U.S. Department Of Energy under Contract No. DE-AC02-09CH11466 with Princeton University, and was granted access to the HPC resources of CINES, under the allocations A00505066912 and A00705066912 made by GENCI.

## Data availability

The data that support the findings of this study are available from the corresponding author upon reasonable request.

## Appendix

### A Forces

The ion drag force is

$$\mathbf{F}_d = \sum_z m_{i,z} n_{i,z} \pi a_d^2 v_{T,i,z} \zeta \left( \frac{u_z - v}{v_{T,i,z}}, \frac{Z\chi}{\tau_z} \right) (\mathbf{u}_z - \mathbf{v}) \quad (\text{A1})$$

with  $\mathbf{u}_z$  the background ion flow velocity,  $n_{i,z}$ ,  $v_{T,i,z}$  and  $m_{i,z}$  the ion density, thermal velocity and mass respectively for the ion species  $z$  with charge  $Z$ , and  $a_d$  is the dust grain radius. The function  $\zeta \left( \frac{u_z - v}{v_{T,i}}, \frac{Z\chi}{\tau_z} \right) \sim 5$ , derived in the framework of the OML theory, detailed in Ref. [10], is given by the sum of a collection and a scattering part  $\zeta = \zeta_{coll} + \zeta_{sc}$ . The collection part is:

$$\zeta_{coll}(U, X)|_{X \geq 0} = \frac{1}{2U^2} \left\{ \frac{1}{\sqrt{\pi}} (1 + 2W_p) \exp(-U^2) + U \left[ 1 + 2W_p - \frac{1}{2U^2} (1 - W_m) \right] \operatorname{erf}(U) \right\} \quad (\text{A2})$$

for a negatively charged dust particle  $\chi > 0$ . In this appendix, we make use of the following quantities:

$$U = \frac{u_z - v}{v_{T,i}}, \quad X = Z\chi/\tau_z, \quad U_{p/m} = U \pm \sqrt{-X}, \quad W_{p/m} = U^2 \pm X \quad (\text{A3})$$

For a positively charged dust particle ( $\chi < 0$ ) it is instead

$$\begin{aligned} \zeta_{coll}(U, X)|_{X < 0} = & \frac{1}{4U^2} \left\{ \frac{1}{\sqrt{\pi}} \left( 1 + 2U^2 + \frac{1 - 2U^2}{U} \sqrt{-X} \right) (\exp -U_p^2 + \exp -U_m^2) \right. \\ & \left. + U \left[ 1 + 2W_p - \frac{1}{2U^2} (1 - 2W_m) \right] [\operatorname{erf}(U_p) + \operatorname{erf}(U_m)] \right\} \end{aligned} \quad (\text{A4})$$

The scattering part of the drag force is

$$\zeta_{sc}(U, X) = X^2 \ln \Lambda \frac{1}{U^3} \left[ \operatorname{erf}(U) - \frac{2}{\sqrt{\pi}} U \exp(-U^2) \right] \quad (\text{A5})$$

with  $\ln \Lambda$  the Coulomb logarithm. The latter is computed following Ref.[9] as

$$\begin{aligned} \ln \Lambda &= \frac{1}{2} \ln \left\{ \frac{b_{90}^2 + (\eta_{fit} \lambda_s)^2}{b_{90}^2 + a_d^2} \right\} \\ b_{90} &= \frac{a_d \chi}{\tau_i (3 + 2U^2)}, \quad \frac{1}{\lambda_s^2} = \frac{1}{\lambda_D^2} \left( 1 + \frac{3}{\tau_i (3 + 2U^2)} \right) \end{aligned} \quad (\text{A6})$$

with  $\lambda_D$  the Debye length. The factor

$$\eta_{fit} = 1 + \frac{a_d}{\lambda_s} \left( 1 + \sqrt{\frac{1}{6\tau_i}} \right) \quad (\text{A7})$$

is meant to extend the validity of the OML drag force to bigger grains, by fitting the the results from Ref. [34].

Similarly to the ion drag force, the drag force from neutrals reads:

$$\mathbf{F}_{d,n} = m_n n_n \pi a_d^2 v_{T,n} \zeta_n \left( \frac{u_n - v}{v_{T,n}} \right) (\mathbf{u}_n - \mathbf{v}) \quad (\text{A8})$$

where  $n_n$ ,  $v_{T,n}$ ,  $m_n$  and the neutral atoms density, thermal velocity and mass respectively,  $\mathbf{u}_n$  is the net neutral flow velocity,  $U_n = \frac{u_n - v}{v_{T,n}}$  and

$$\zeta_n(U_n) = \frac{1}{U_n} \left\{ \frac{1}{\sqrt{\pi}} \left( U_n + \frac{1}{U_n} \right) \exp(-U_n^2) + \left( 1 + U_n^2 - \frac{1}{4U_n^2} \operatorname{erf}(U_n) \right) \right\} \quad (\text{A9})$$

The electric force on the dust grain with charge  $eq_d/a_d = \chi T_e$  is  $\mathbf{F}_E = q_d \mathbf{E}$ .

The gravitational force is  $\mathbf{F}_g = m_d g$ .

The centrifugal (apparent) force, arising in our cylindrical frame of reference  $(R, Z, \phi)$ , is  $\mathbf{F}_c = m_d(-v_\phi^2/R, 0, v_R v_\phi/R)$ .

## B Currents

The total ion current is

$$I_i = \sum_z e \pi a_d^2 n v_{T,i,z} F_i \left( \frac{u - v}{v_{T,i,z}}, \frac{Z\chi}{\tau_z} \right) \quad (\text{B1})$$

The factor  $F_i$ , derived in the framework of OML theory, can be found in Ref. [10]. For a negatively charged dust particle  $\chi > 0$  it reads

$$F_i(U, X)|_{X \geq 0} = \frac{1}{2U} \{ [1 + 2(U^2 + X)] \operatorname{erf}(U) + \frac{2U}{\sqrt{\pi}} \exp(-U^2) \} \quad (\text{B2})$$

where  $U$ ,  $X$ ,  $U_p$ ,  $U_m$  have been defined previously in Eq. (A3). For a positively charged dust particle ( $\chi < 0$ ) it is instead

$$F_i(U, X)|_{X < 0} = \frac{1}{4U} \{ [1 + 2(U^2 + X)] [\operatorname{erf}(U_p) + \operatorname{erf}(U_m)] + \frac{2}{\sqrt{\pi}} [U_p \exp(-U_m^2) + U_m \exp(-U_p^2)] \} \quad (\text{B3})$$

The electron current is

$$I_e = -e 4 \pi a_d^2 n \sqrt{v_{T,e}^2 / 2\pi} F_e(\chi) \quad (\text{B4})$$

where the electrons are assumed to have a Maxwellian distribution with temperature  $T_e$ , resulting in  $F_e(\chi) = 1 - \chi$  for  $\chi < 0$  and  $F_e(\chi) = \exp(-\chi)$  for  $\chi > 0$ .

The thermionic electron emission from the heated dust is

$$I_{th} = e 16 \pi a_d^2 T_d^2 / h^3 \exp(-W_f/T_d) F_{th} \quad (\text{B5})$$

where  $W_f$  is the dust material work function,  $W_f = 4.6$  eV for carbon [9], and  $F_{th} = 1$  for negatively charged dust ( $\chi > 0$ ) and  $F_{th} = (1 - \chi e T_e / k_b T_d) \exp(\chi e T_e / k_b T_d)$  for positively charged dust ( $\chi < 0$ ). The secondary electron emission current is

$$I_{SEE} = I_e \frac{2}{2 - \beta} F_{SEE} \quad (\text{B6})$$

where  $\beta$  is a material dependent parameter [14],  $F_{SEE} = F_{YD}(T_e, \chi = 0)$  for  $\chi \geq 0$  and  $F_{SEE} = F_{YD}(T_e, \chi) \frac{1 - 3\chi T_e / W_f}{(1 - \chi)(1 - \chi T_e / W_f)^3 \exp(-\chi)}$  for  $\chi < 0$ , which is a representation of the Young-Dekker formula [42, 43], described in details in Ref. [17].

## C Heat fluxes

The heat fluxes associated with the impinging ion flux is

$$W_i = \sum_z \pi a_d^2 n_{i,z} v_{T,i,z} T_{i,z} G_i \left( \frac{u - v}{v_{T,i,Z}}, \frac{Z\chi}{\tau_z} \right) \quad (\text{C1})$$

The factor  $G_i$ , derived in the framework of OML theory, can be found in Ref. [10]. For a negatively charged dust particle  $\chi > 0$  it reads

$$\begin{aligned} G_i(U, X)|_{X \geq 0} = & \frac{1}{4} \left\{ \frac{2}{\sqrt{\pi}} \left[ 5 + 2(U^2 + X) \right] \exp(-U^2) \right. \\ & \left. + \frac{1}{U} \left[ 3 + 12U^2 + 4U^4 + 2X(1 + 2U^2) \right] \operatorname{erf}(-U^2) \right\} \end{aligned} \quad (\text{C2})$$

where  $U$ ,  $X$ ,  $U_p$ ,  $U_m$  have been defined previously in Eq. (A3). For a positively charged dust particle ( $\chi < 0$ ) it is instead

$$\begin{aligned} G_i(U, X)|_{X < 0} = & \frac{1}{8} \left\{ \frac{2}{\sqrt{\pi}} \left[ \left( 5 + 2U^2 - \frac{3 + 2U^2}{U} \sqrt{-X} \right) \exp(-U_p^2) \right. \right. \\ & + \left( 5 + 2U^2 + \frac{3 + 2U^2}{U} \sqrt{-X} \right) \exp(-U_m^2) \\ & \left. \left. + \frac{1}{U} \left[ 3 + 12U^2 + 4U^4 + 2X(1 + 2U^2) \right] \operatorname{erf}(-U^2) [\operatorname{erf}(U_p) + \operatorname{erf}(U_m)] \right\} \right\} \end{aligned} \quad (\text{C3})$$

The electron heat flux is [17]

$$W_e = T_e (I_e/e) G_e(\chi) \quad (\text{C4})$$

with  $G_e = 2 + \chi$  for  $\chi > 0$  and  $G_e = (2 - \chi)/(1 - \chi)$  for  $\chi < 0$ .

The heat fluxes associated with the loss of electrons through thermionic emission is

$$\begin{aligned} W_{th}|_{\chi \geq 0} = & W_{th,p} = (W_f + 2T_d k_b/e) I_{th}/e \\ W_{th}|_{\chi < 0} = & \frac{1}{2} W_{th,p} \left[ 2 - \frac{2\chi e T_e}{k_b T_d} + \left( \frac{\chi e T_e}{k_b T_d} \right)^2 \right] \exp \left( \frac{\chi e T_e}{k_b T_d} \right) \end{aligned} \quad (\text{C5})$$

The heat fluxes associated with secondary electron emission is [10, 14]

$$\begin{aligned} W_{SEE}|_{\chi \geq 0} = & 3W_f I_{SEE}/e \\ W_{SEE}|_{\chi < 0} = & 3W_f \frac{\left( 1 - \frac{\chi T_e}{W_f} \right) \left( 1 - 2\frac{\chi T_e}{W_f} \right)}{1 - 3\frac{\chi T_e}{W_f}} I_{SEE}/e \end{aligned} \quad (\text{C6})$$

The radiative cooling is

$$W_{bb} = 4\pi a_d^2 \sigma_{SB} \epsilon (T_d^4 - T_w^4) \quad (\text{C7})$$

where  $T_w$  is the first wall temperature and  $\epsilon$  is the dust grain emissivity ( $\epsilon = 0.75$  for carbon [44]). The heat flux associated with the evaporation of the dust grain is

$$W_{ev} = 4\pi a_d^2 P_{vap}(T_d)/\sqrt{2\pi m_I k_b T_d m_I h_{sub}}/e \quad (\text{C8})$$

with  $h_{ev}$  the evaporation heat,  $m_I$  the mass of the sublimated impurities, and

$$P_{vap}[\text{Pa}] = 10^{A/T_d + B} \quad (\text{C9})$$

is the vapor pressure [10],  $T_d$  is in K and  $A$  and  $B$  two material dependent constants.

## D Mass balance

The only term we consider in Eq. (4) is the evaporation flux

$$\Gamma_{ev} = -4\pi a_d^2 P_{vap}(T_d) / \sqrt{2\pi m_I k_b T_d} \quad (\text{D1})$$

with  $P_{vap}$  defined in Eq. (C9).

## References

- [1] P.C. Stangeby . **Assessing material migration through  $^{13}\text{C}$  injection experiments.** *Journal of Nuclear Materials*, **415**, 2011.
- [2] Andrea Uccello, Gabriele Gervasini, Francesco Ghezzi, Enzo Lazzaro, D. Borodin, I. Borodkina, D. Douai, A. Huber, I. Jepu, D. Terranova, A. Widdowson and JET Contributors . **An insight on beryllium dust sources in the JET ITER-like wall based on numerical simulations.** *Plasma Physics and Controlled Fusion*, **62**:064001, 2020.
- [3] A. Bortolon, V. Rohde, R. Maingi, E. Wolfrum, R. Dux, A. Herrmann, R. Lunsford, R.M. McDermott, A. Nagy, A. Kallenbach, D.K. Mansfield, R. Nazikian, R. Neu, and the ASDEX Upgrade team. **Real-time wall conditioning by controlled injection of boron and boron nitride powder in full tungsten wall ASDEX Upgrade.** *Nuclear Materials and Energy*, **19**:384–389, 2019.
- [4] R. Maingi , J.S. Hu, Z. Sun, K. Tritz, G.Z. Zuo, W. Xu, M. Huang, X.C. Meng, J.M. Canik, A. Diallo, R. Lunsford, D.K. Mansfield, T.H. Osborne, X.Z. Gong, Y.F. Wang , Y.Y. Li and EAST team. **ELM elimination with Li powder injection in EAST discharges using the tungsten upper divertor.** *Nuclear Fusion*, **58**:024003, 2018.
- [5] R. Lunsford , V. Rohde, A. Bortolon , R. Dux, A. Herrmann, A. Kallenbach , R.M. McDermott , P. David, A. Drenik, F. Laggner, R. Maingi, D. K. Mansfield, A. Nagy, R. Neu, E. Wolfrum and the ASDEX Upgrade team. **Active conditioning of ASDEX Upgrade tungsten plasma-facing components and discharge enhancement through boron and boron nitride particulate injection.** *Nuclear Fusion*, **59**:126034, 2019.
- [6] F. Nespoli, N. Ashikawa, E.P. Gilson, R. Lunsford, S. Masuzaki, M. Shoji, T. Oishi, C. Suzuki, A. Nagy, A. Mollen, N.A. Pablant, K. Ida, M. Yoshinuma, N. Tamura, D.A. Gates, T. Morisaki, the LHD experiment group . **First impurity powder injection experiments in LHD.** *Nuclear Materials and Energy*, **25**:100842, 2020.
- [7] R. Lunsford, C. Killer, A. Nagy, D. Gates, T. Klinger, A. Dinklage, S. Lazerson, F. Nespoli, N. A. Pablant, G. Satheeswaran, et al. . **Characterization of injection and confinement improvement through impurity induced profile modifications on the Wendelstein 7-X stellarator.** *Physics of Plasmas*, :submitted for publication, 2021.
- [8] L.R. Baylor, S.J. Meitner, T.E. Gebhart, J.B.O. Caughman, J.L. Herfindal, D. Shiraki and D.L. Youchison. **Shattered pellet injection technology design and characterization for disruption mitigation experiments.** *Nuclear Fusion*, **59**:066008, 2019.
- [9] A.Yu. Pigarov and S.I. Krasheninnikov . **Dust-particle transport in tokamak edge plasmas.** *Physics of Plasmas*, **12**:122508, 2005.

- [10] R.D. Smirnov, A Yu Pigarov, M Rosenberg, S I Krasheninnikov and D A Mendis. **Modelling of dynamics and transport of carbon dust particles in tokamaks.** *Plasma Physics and Controlled Fusion*, **49**:347–371, 2007.
- [11] E. Lazzaro, I Proverbio, F Nespoli, S Ratynskaia, C Castaldo, U deAngelis, M DeAngelis, J-P Banon and L Vignitchouk . **Transport and effects of ferromagnetic dust in a tokamak with a metallic vessel.** *Plasma Physics and Controlled Fusion*, **54**:124043, 2012.
- [12] G. Gervasini, E. Lazzaro and A. Uccello . **Physical and Numerical Model for Calculation of Ensembles of Trajectories of Dust Particles in a Tokamak.** *Journal of Fusion Energy*, **36**:25–29, 2017.
- [13] S. Ratynskaia, L. Vignitchouk, P. Tolias, I. Bykov, H. Bergsåker, A. Litnovsky, N. den Harder and E. Lazzaro. **Migration of tungsten dust in tokamaks: role of dust–wall collisions.** *Nuclear Fusion*, **53**:123002, 2013.
- [14] L. Vignitchouk, P Tolias and S Ratynskaia . **Dust–wall and dust–plasma interaction in the MIGRAINE code.** *Plasma Physics and Controlled Fusion*, **56**:095005, 2014.
- [15] M. Bacharis and M. Coppins . **Critical issues for modeling dust transport in tokamaks.** *Physical Review E*, **82**:026403, 2010.
- [16] A. Autricque, S.H. Hong, N. Fedorczak, S.H. Son, H.Y. Lee, d , I. Song, W. Choe, C. Grisolia . **Simulation of W dust transport in the KSTAR tokamak, comparison with fast camera data.** *Nuclear Materials and Energy*, **12**:599–604, 2017.
- [17] A. Autricque . **Dust transport in tokamaks.** *PhD Thesis*, :<https://www.theses.fr/2018AIXM0315.pdf>, 2018.
- [18] M. Shoji, G. Kawamura, R. Smirnov, Y. Tanaka, S. Masuzaki, Y. Uesugi, N. Ashikawa, E. Gilson, R. Lunsford. **Full-torus impurity transport simulation for optimizing plasma discharge operation using a multi-species impurity powder dropper in the large helical device.** *Contributions to Plasma Physics*, :e201900101, 2019.
- [19] P. Tamain, H.Bufferanda, G.Ciraolo, C.Colin, D.Galassi, Ph.Ghendrih, F.Schwander, E.Serre. **The TOKAM3X code for edge turbulence fluid simulations oftokamak plasmas in versatile magnetic geometries.** *Journal of Computational Physics*, **321**:606–623, 2016.
- [20] H.M Mott and I. Langmuir. **The theory of collectors in gaseous discharges.** *Physical Review*, **28**:727–763, 1926.
- [21] E. Lazzaro, G Gervasini, F Ghezzi, A Uccello and JET contributors1. . **Rocket effect on dust particles in the tokamak SOL.** *Physica Scripta*, **95**:055605, 2020.
- [22] A. Autricque, N. Fedorczak, S. A. Khrapak, L. Couedel, B. Klumov, C. Arnas, N. Ning, J.-M. Layet, and C. Grisolia . **Magnetized electron emission from a small spherical dust grain in fusion related plasmas.** *Physics of Plasmas*, **24**:124502, 2017.
- [23] Camille Baudoin, Patrick Tamain, Hugo Bufferand, Guido Ciraolo, Nicolas Fedorczak, Davide Galassi, Philippe Ghendrih, Nicolas Nace . **Turbulent heat transport in TOKAM3X edge plasma simulations.** *Contributions to Plasma Physics*, **58**:484–489, 2018.

- [24] R. Tatali, Eric Serre, Patrick Tamain, Davide Galassi, Philippe Ghendrih, Federico Nespoli, Hugo Bufferand, Thomas Cartier-Michaud and Guido Ciraolo. **Impact of collisionality on turbulence in the edge of tokamak plasma using 3D global simulations.** *Nuclear Fusion*, <https://doi.org/10.1088/1741-4326/abe98b>:accepted for publication, 2021.
- [25] S J Zweben, J A Boedo, O Grulke, C Hidalgo, B LaBombard, R J Maqueda, P Scarin, and J L Terry. Edge turbulence measurements in toroidal fusion devices. *Plasma Physics and Controlled Fusion*, 49(7):S1–S23, jun 2007.
- [26] P. Siegle, I. Goychuk, and P. Hanggi . **Origin of Hyperdiffusion in Generalized Brownian Motion.** *Physical Review Letters*, **105**:100602, 2010.
- [27] P. Siegle, I. Goychuk, and P. Hanggi. **Markovian embedding of non-Markovian superdiffusion.** *Physical Review E*, **81**:011136, 2010.
- [28] R. Kubo . **The fluctuation-dissipation theorem.** *Reports on Progress in Physics*, **25**:255, 1966.
- [29] K. Gustavsson and B. Mehlig . **Distribution of velocity gradients and rate of caustic formation in turbulent aerosols at finite Kubo numbers.** *Physical Review E*, **87**:023016, 2013.
- [30] F. Nespoli, P. Tamain, N. Fedorczak, G. Ciraolo, D. Galassi, R. Tatali, E. Serre, Y. Marandet, H. Bufferand and Ph. Ghendrih. **3D structure and dynamics of filaments in turbulence simulations of WEST diverted plasmas.** *Nuclear Fusion*, **59**:096006, 2019.
- [31] J.A. Krommes . **Introductory Lectures on Plasma Kinetic Theory, Turbulence, and Transport Volume I: Weakly Coupled Kinetic Theory and Classical Transport.** *in preparation*, 2019.
- [32] John A. Krommes. A tutorial introduction to the statistical theory of turbulent plasmas, a half-century after kadomtsev's plasma turbulence and the resonance-broadening theory of dupree and weinstock. *Journal of Plasma Physics*, 81(6):205810601, 2015.
- [33] Y. Marandet, N Nace, M Valentinuzzi, P Tamain, H Bufferand, G Ciraolo, P Genesio and N Mellet . **Assessment of the effects of scrape-off layer fluctuations on first wall sputtering with the TOKAM-2D turbulence code.** *Plasma Physics and Controlled Fusion*, **58**:114001, 2016.
- [34] I.H. Hutchinson . **Ion collection by a sphere in a flowing plasma: 3. Floating potential and drag force.** *Plasma Physics and Controlled Fusion*, **47**:71, 2004.
- [35] J.S. Chang and K. Spariosu . **Dust particle charging characteristics under a collisionless magneto-plasma.** *Journal of the Physical Society of Japan*, **62**:97–104, 1993.
- [36] L. James and M. Coppins . **Suppression of the ion drag force on dust in magnetized plasmas.** *Physics of Plasmas*, **27**:063704, 2020.
- [37] S.I. Krasheninnikov and R.D. Smirnov . **Dust in magnetic fusion devices.** *Plasma Physics and Controlled Fusion*, **53**:083001, 2011.
- [38] S.I. Krasheninnikov and R.D. Smirnov . **On interaction of large dust grains with fusion plasma.** *Physics of Plasmas*, **16**:114501, 2009.

- [39] E. D. Marenkov and S. I. Krasheninnikov. **Ablation of high-Z material dust grains in edge plasmas of magnetic fusion devices.** *Physics of Plasmas*, **21**:123701, 2014.
- [40] S.I. Krasheninnikov and E.D. Marenkov. On ablation of large tungsten dust grains in edge plasma of fusion devices. *Journal of Nuclear Materials*, 463:869–872, 2015. PLASMA-SURFACE INTERACTIONS 21.
- [41] R. D. Smirnov and S. I. Krasheninnikov. **Time-dependent modeling of dust outburst into tokamak divertor plasma.** *Physics of Plasmas*, **27**:082509, 2020.
- [42] J.R. Young . . *Journal of Applied Physics*, **28**:524, 1957.
- [43] A.J. Dekker . . *Solid State Physics*, **6**:251, 1958.
- [44] G. Federici, A Loarte and G Strohmayer. **Assessment of erosion of the ITER divertor targets during type I ELMs.** *Plasma Physics and Controlled Fusion*, **45**:1523, 2003.